Research Article Vol. 30, No. 5 / 28 Feb 2022 / Optics Express 8049
Optics EXPRESS

Tailoring bound states in the continuum in symmetric photonic crystal slabs by coupling strengths

ZHAOJIAN ZHANG,[1] JUNBO YANG,[1,2,*] TE DU,[1] HANSI MA,[3] AND XINPENG JIANG[1]

[1] College of Liberal Arts and Sciences, National University of Defense Technology, Changsha 410073, China
[2] Center of Material Science, National University of Defense Technology, Changsha 410073, China
[3] Institute for Quantum Information & State Key Laboratory of High Performance Computing, College of Computer Science, National University of Defense Technology, Changsha 410073, China
[*] yangjunbo@nudt.edu.cn

Abstract: In this work, we investigate polarization-insensitive dual bound states in the continuum (BICs) at Γ point in symmetric photonic crystal (PhC) slabs. Especially, BICs are tailored by tuning intra- and intercellular optical coupling strengths of PhC slabs. Based on four different approaches, we realize the transition from BIC to quasi-BIC resonances with various dispersion behaviors while maintaining the symmetry of slabs. Also, we show the two resonances are lowest-order even and odd eigenmodes that can match the symmetry of the incident plane wave, and their quality (Q) factors follow the inverse quadratic law except for cases with larger perturbations. Furthermore, multipolar decomposition reveals that even quasi-BICs are dominated by the toroidal dipole and magnetic quadrupole, while odd quasi-BICs are governed by the magnetic dipole and electric quadrupole. Interestingly, an anomalous increase of the Q factor is observed in one case, which is attributed to the mode transformation. Finally, anisotropic coupling adjustment is discussed, which enriches the degrees of freedom to manipulate BICs. This work introduces a novel perspective to tailor BICs at Γ point in PhC slabs and has potential planar photonic applications for nonlinear enhancement and sensing.

1. Introduction

Resonances with high-quality (Q) factors play an important role in photonics due to the promising capability to dramatically enhance the light-matter interaction, which introduces various applications such as slow-light devices [1], nonlinear-effect enhancement [2], sensing with ultra-high sensitivity [3], and low-threshold lasing [4]. Different photonic platforms prefer high-Q resonances with different forms. For example, whispering-gallery modes (WGMs) always serve as high-Q resonances in on-chip photonic circuits [5,6]. In planar dielectric metasurfaces, there exist localized Mie resonances with finite Q factors [7,8]. In photonic crystals (PhCs), light can be well confined in PhC cavities with band gaps [9,10]. However, on-chip WGM resonances possess much higher Q factors than Mie resonances in metasurfaces, because the former is well-confined by total internal reflection, while the latter is above the light line, where the resonance is naturally radiative. Similar contrast occurs between PhC cavity resonances stimulated by in- or out-of-plane excitations, since the resonance will also be above the light line when the excitation is near the Γ point [11,12].

Recently, bound states in the continuum (BICs) have provided a solution to create high-Q resonances beyond the light line. Originally introduced in quantum mechanics to describe the discrete eigenstates of Schrödinger equations embedded in the continuous energy states [13], BICs then are extended to photonics and regarded as perfect resonant modes with infinite Q factor existing in the radiative continuum, namely, above the light line [14,15]. One type of BICs emerges

#454408 https://doi.org/10.1364/OE.454408
Journal © 2022 Received 24 Jan 2022; revised 14 Feb 2022; accepted 14 Feb 2022; published 23 Feb 2022

Optics EXPRESS

in the k space of PhCs due to accidental destructive interferences between different resonances, called accidental or resonance-trapped BICs [16,17]. Another case is symmetry-protected BICs located at Γ point, resulting from the complete decoupling between resonances and radiative channels due to symmetry mismatch [18]. Especially, by fine-breaking the structural symmetry, ideal symmetry-protected BICs can be transformed into leaky quasi-BICs, which provides a convenient approach to get high-Q resonances in metasurfaces and PhC slabs [18–21]. As a side effect, such asymmetry will essentially make quasi-BICs polarization-sensitive. To overcome this drawback, supercell metasurfaces with specifically arranged unit cells with C_4 symmetry are proposed [22–25], and a similar scheme is also worth exploring in PhCs.

Originally proposed to describe elementary excitations in linear conjugated polymers, the one-dimensional (1D) Su-Schrieffer-Heeger (SSH) model serves as one of the most important models to feature topological behaviors [26]. Generally speaking, it describes band dynamics based on intra- and intercellular hopping parameters, and the fine-tuning of these parameters can make band structures change continuously. The 1D SSH model, together with its extended 2D case, has been extensively employed in topological photonics [27,28]. In particular, the 2D SSH model has been introduced to PhCs [29–31]. As an analogue, rods or holes of PhCs play the role of atoms in the 2D SSH model, and hopping parameters can be altered by tuning coupling strengths between neighboring rods or holes of PhCs. This scheme not only enables the continuous change of states, but also ensures the isotropic topological transition due to the preservation of C_4 symmetry. Thus, inspired by this model, we wonder if it is feasible to adopt the coupling strength as a parameter to induce the leakage of BICs in symmetric structures, meanwhile maintaining the structural symmetry.

In this work, we theoretically investigate BIC and quasi-BIC resonances in symmetric PhC slabs at Γ point by tuning the intracellular and intercellular optical coupling strengths based on four different approaches inspired by the 2D SSH model. Since our PhC slabs maintain C_4 symmetry during the adjustment, these quasi-BIC resonances are polarization-insensitive. Further study shows that these resonances are lowest-order eigenmodes that can match the symmetry of the incident plane wave, and can be classified by even and odd parity with respect to the horizontal mirror plane of the slab. Q factor analysis reveals that these resonances follow the inverse quadratic law except for cases with large perturbations. Furthermore, multipole decomposition indicates that even quasi-BIC resonances are dominated by the toroidal dipole and magnetic quadrupole, while odd quasi-BIC resonances are governed by the magnetic dipole and electric quadrupole. The physical mechanisms behind the anomalous behaviors of the Q factor are also revealed by multipole contributions. Finally, we discuss the PhC cases under the isotropic coupling strengths, as well as influences of material losses and substrates. This work provides novel approaches to tailor Γ-point polarization-insensitive BICs in symmetric PhC slabs, and can be applied as high-Q cavities in planar photonic devices for double-resonant nonlinear enhancement, multi-spectral sensing, and lasing.

2. Geometrical configuration and 2D SSH model

The geometrical configuration of the proposed dielectric PhC slab as a platform to implement BICs is presented in Fig. 1(a). It consists of a periodic arrangement of PhC unit cells, each of which is composed of four air holes. The lattice constant of the unit cell is $a = 1$ μm, the thickness of the slab is $H = 0.5a$, and the permittivity is $\varepsilon = 12$. As depicted in Fig. 1(a), the plane wave with x-polarization incidents vertically on the PhC slab as a far-field excitation. The schematic of the 2D SSH model is introduced in Fig. 1(b). There are four atoms in one unit cell of the lattice, and the intracellular (between atoms in the same unit cell) and intercellular (between atoms in adjacent unit cells) hoppings are represented by red and green bonds, respectively. The corresponding amplitudes are t_a and t_b, respectively. In our PhC slabs as shown in Fig. 1(a) and (c), the four air holes play the role of the four atoms in one unit cell of 2D SSH model, and

Optics EXPRESS

adjusting the distances between neighboring holes in the same and adjacent unit cells (d_a and d_b, indicated by red and green arrows in Fig. 1(c)) changes the intracellular and intercellular optical coupling strengths, respectively, which is the analogue of tuning hopping amplitudes in the 2D SSH model [29–31].

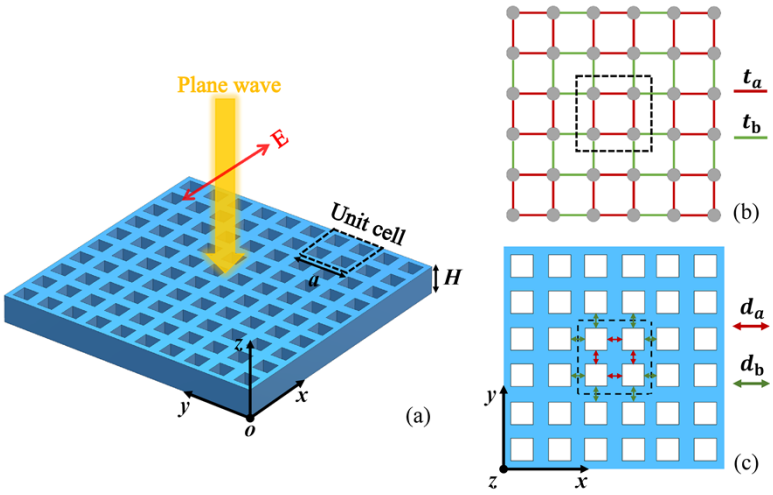

Fig. 1. (a) The geometric configuration of the PhC slab. The PhC slab consists of periodically arranged unit cells along x and y directions, which include four air holes. There is an x-polarized plane wave that incidents on the PhC slab along z-axis. (b) The schematic of 2D SSH model on a square lattice with hopping in each direction. There are four atoms in one unit cell, which are represented by grey dots. The red and green bonds represent the intracellular and intercellular hoppings, respectively. The amplitudes of them are t_a and t_b, respectively. (c) The schematic of the PhC slab in the x-y plane. There are four air holes in one unit cell. The blue and white areas represent dielectric and air, respectively. The red and green arrows represent the intracellular and intercellular distances, respectively, which can indicate the coupling strengths. The corresponding values are d_a and d_b, respectively.

There are several typical approaches to implement the adjustment of the intracellular and intercellular coupling strengths. The first one is to move the centers of the four air holes inwardly or outwardly along the diagonals of the unit cell as shown in Fig. 2(a), so that d_a and d_b are changed at the same time [29]. The second approach, which possesses one air hole at the center and four air holes at the corners in one unit cell, focuses on expanding the length of the central air hole l_a meanwhile shrinking the length of the corner air holes l_b [31]. In this way, intracellular and intercellular coupling strengths are tuned simultaneously in a different manner. Based on the first approach, we can also choose to change only the intercellular coupling strength by tuning d_b meanwhile keeping d_a unchanged as indicated in Fig. 2(c), or change only the intracellular coupling strength by tuning d_a meanwhile keeping d_b unchanged as shown in Fig. 2(d) [30]. In the next section, we will adopt the schemes mentioned above to manipulate Γ-point BICs in the proposed PhC slabs.

The full-wave simulation is implemented based on the Finite Difference-Time Domain (FDTD) method. In the simulated domain, the unit cell is established with periodic conditions in the $\pm x$ and $\pm y$ directions, and perfectly matched layers (PMLs) are set in the $\pm z$ directions. The plane wave source is introduced on the top of the unit cell and propagates towards -z direction as presented in Fig. 1(a), so that the modes of PhC slabs can be excited at Γ point. A 2D power monitor across the x-y plane is placed under the unit cell, and the total transmitted power P_t

Optics EXPRESS

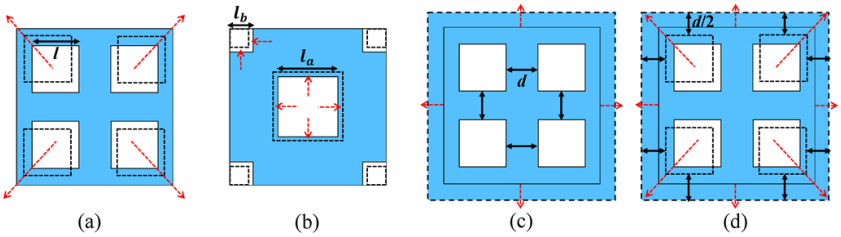

Fig. 2. The schematics for the four approaches to tune the intracellular and intercellular coupling strengths. The red arrows indicate the direction of moving, expanding or shrinking, and the black dash lines indicate the profiles of holes or slabs after the adjustment. (a) Moving the centers of the four air holes inwardly or outwardly along the diagonals of the unit cell. Here, the length of air holes is kept at $l = 0.3$ μm. (b) expanding the length of the central air hole l_a meanwhile shrinking the length of the corner air holes l_b. (c) Tuning d_b meanwhile keeping $d_a = d = 0.2$ μm. This case can be realized by tuning only the lattice constant a. Here, $l = 0.3$ μm. (d) Tuning d_a meanwhile keeping $d_b = d = 0.2$ μm. This case can be realized by simultaneously tuning the positions of the four air holes in one unit cell as well as the lattice constant a. Here, $l = 0.3$ μm.

is extracted by integrating the power across the monitor surface. The normalized transmission spectra are calculated by $T(\omega) = P_t(\omega)/P_s(\omega)$, where P_s is the power of the light source.

3. Spectral properties of BICs in proposed PhC slabs

The transmission spectra of the PhC slab following the approach in Fig. 2(a), namely, the first PhC case, are shown in Fig. 3(a). It is shown that there is no transmission dip when $d_a = d_b = d = 0.2$ μm, where we define d as the critical point for the distance, which represents the critical point for the coupling strength. However, after we move the four air holes inwardly or outwardly along the diagonals of the unit cell, that is, decrease or increase d_a (meanwhile d_b is also changed), two transmission dips appear in the spectrum, showing the formation of two resonances. Besides, as d_a (d_b) varies away from the critical point, the resonant frequencies of the two resonances shift continuously and symmetrically, and the corresponding linewidths of the two resonances turn to be wider, which means the two resonances become leakier. It is indicated that there are two perfect non-leaky resonances at the critical point, which are BIC resonances. The resonances at non-critical points are quasi-BIC resonances which are leaky due to the modification of the intracellular and intercellular coupling strengths. In addition, the two resonances can be classified as even or odd modes in PhC slabs respectively as indicated by the red and green dash curves in Fig. 3(a), which means they are even or odd with respect to the horizontal mirror plane of the slab [32]. In spectra, the frequencies of the two modes cross and do not couple to each other, which further proves that they are orthogonal. What is more, the eigenmode calculation reveals that the two resonances are the lowest-order even and odd eigenmodes that can match the spatial symmetry of the incident plane wave, which is odd under 180° rotation around the z-axis. It is worth noting that such parity classification and eigenmode conclusion still hold for the other three PhC cases that will be shown below. The details of parity definition and eigenmode solutions are provided in Appendix A.

Following the scheme in Fig. 2(b), the corresponding transmission spectra are shown in Fig. 3(b). Here, the critical point is $l_a = l_b = l = 0.3$ μm, and we shrink or expand the two parameters meanwhile keep the condition $l_a + l_b = 0.6$ μm fulfilled. In this case, the even and odd resonances become BICs at the critical point and quasi-BICs at non-critical points, respectively. Their resonant frequencies possess different dispersive manners from the first PhC case, whereas

Optics EXPRESS

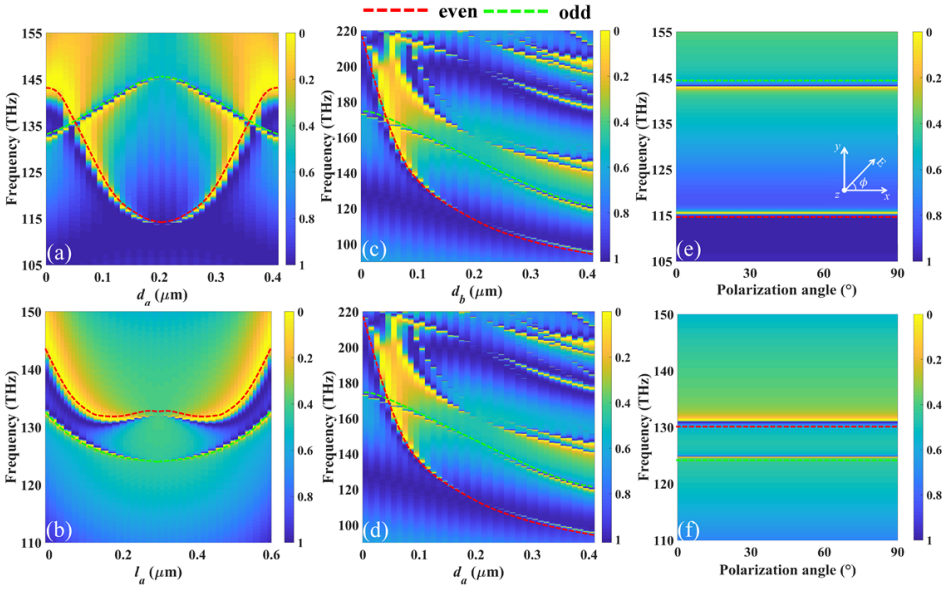

Fig. 3. (a-d) The transmission spectra under different intracellular and intercellular coupling strengths following approaches from Fig. 2(a) to (d). (e) The transmission spectra under different polarization angles for the first approach with $d_a = 0.25$ μm. The inset shows the definition of the polarization angle. (f) The transmission spectra under different polarization angles for the second approach with $l_a = 0.39$ μm. The red and green dash curves indicate the frequency dispersions of even and odd BIC resonances, respectively.

are also symmetric with respect to the critical point. The transmission spectra for approaches in Fig. 2(c) and (d) are shown in Fig. 3(c) and (d), respectively. Herein, the critical point is also at $d_a = d_b = d = 0.2$ μm, and only d_b or d_a is changed in each case. It is shown that these two approaches can also effectively transfer the two BIC resonances into quasi-BIC resonances, meanwhile endowing them with different frequency dispersions. Notably, these two cases possess the same pictures in spectra. It is because these two approaches are identical if we shift the center of the unit cell in one case by half a lattice constant.

For the first PhC case with $d_a = 0.25$ μm where the two BICs are leaky, we further study the corresponding transmission spectra under different polarization angles ϕ of the incident wave defined in the inset of Fig. 3(e). As shown in Fig. 3(e), resonant frequencies of the two quasi-BICs are independent of the polarization angle. It is because the first approach to tune the coupling strength does not break the C_4 symmetry of the PhC slab, which is also applied for the other approaches in Fig. 2. For example, the transmission spectra under different polarization angles for the second PhC case with $l_a = 0.39$ μm are presented in Fig. 3(f), where the two quasi-BICs are also polarization-insensitive.

4. Q factor analysis for BICs

Previous studies have revealed that the Q factor of BICs in symmetry-breaking metasurfaces has an inverse quadratic law with the asymmetry parameter α [18,33]:

$$Q = m \cdot \frac{cS}{\omega_0 \cdot \alpha^2} \tag{1}$$

where m is a constant real parameter, c is the speed of light in vacuum, S denotes the area of a unit cell, and ω_0 refers to the resonant frequency of the quasi-BIC resonance. To investigate

Optics EXPRESS

BICs in our symmetric PhC slab, we also refer to this law since the asymmetry parameter can be related to coupling strength parameters in our structure. Here, α is defined as $(d_a - d)/d$ for the first PhC case, and $(l_a - l)/l$ for the second PhC case. Since the third and fourth PhC cases have identical features, we only study the third case in the following sections and the corresponding α is defined as $(d_b - d)/d$. The Q factor is calculated by fitting the transmission spectrum with the Fano formula [34]:

$$T_{Fano} = \left| a_1 + ia_2 + \frac{b}{\omega - \omega_0 + i\gamma} \right|^2 \tag{2}$$

Here, a_1, a_2, and b are constant real parameters and γ is the damping rate of the quasi-BIC resonance. The Q factor can be extracted following the equation $Q = \omega_0/2\gamma$.

For the first and second PhC cases given in Fig. 2(a) and (b), the corresponding Q factors extracted from numerical results as a function of α are plotted as dots in Fig. 4(a) and (b), respectively, and dash curves are fitting results according to Eq. (1). It is shown that the Q factor follows the inverse quadratic law well except for larger α values. It is because Eq. (1) is based on the assumption that the asymmetry-induced perturbation is small [18,33]. In addition, for both cases, it is indicated that the Q factor evolution is symmetric with respect to $\alpha = 0$, and odd quasi-BIC resonances always possess higher Q factors than even quasi-BIC resonances at any non-zero α values. However, in the third PhC case as given in Fig. 2(c), the distribution of Q factors for BIC resonances has a distinct feature, which is asymmetric with respect to $\alpha = 0$ as shown in Fig. 4(c). At larger negative values of α, an anomalous increase of Q factors emerges for even quasi-BIC resonances, and a slight fluctuation of Q factors occurs for odd quasi-BIC resonances. By contrast, the Q factor is finely consistent with the inverse quadratic law for positive α values. Reasons for these behaviors of the Q factor in the third PhC case will be discussed in the next section. In addition, we also investigate field distributions of these quasi-BIC resonances at different α values, which are presented in Supplement 1.

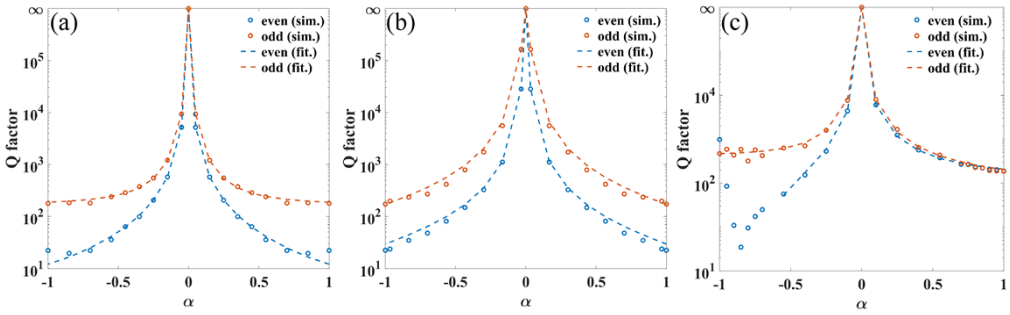

Fig. 4. (a-c) The Q factor of even and odd BIC resonances as a function of α for the first, second, and third PhC cases, respectively.

5. Multipole analysis for BICs

To gain more insight into the origin of BICs in our PhC slabs, we implement the multipole decomposition under the Cartesian coordinate, which is a typical approach to explain the physical mechanism of BICs [35]. It is known that the total extinction cross-section of nanoparticles can be decomposed as the sum of the contributions from multipole moments as follows [36–38]:

$$\begin{aligned} C_{sca}^{total} &= C_{sca}^{p} + C_{sca}^{T} + C_{sca}^{m} + C_{sca}^{Q^e} + C_{sca}^{Q^m} + \dots \\ &= \frac{k^4}{6\pi\varepsilon_0^2 |\mathbf{E}_0|^2} \left[\sum_{\alpha} \left(|p_\alpha + ikT_\alpha|^2 + \frac{|m_\alpha|^2}{c} \right) + \frac{1}{120} \sum_{\alpha\beta} \left(|kQ_{\alpha\beta}^e|^2 + \left| \frac{kQ_{\alpha\beta}^m}{c} \right|^2 \right) + \dots \right] \end{aligned} \tag{3}$$

Optics EXPRESS

where p_α, T_α, and m_α are electric dipole (ED), toroidal dipole (TD), and magnetic dipole (MD) moments, respectively. $Q^e{}_{\alpha\beta}$ and $Q^m{}_{\alpha\beta}$ are electric quadrupole (EQ) and magnetic quadrupole (MQ) moments, respectively. The detailed expressions for multipole moments can be found in [36–38]. $|\mathbf{E}_0|$ represents the electric field amplitude of the input plane wave, and k is the wavenumber. ε_0 refers to the vacuum permittivity, and α, $\beta = x$, y, z. Here, we choose the quasi-BIC resonances in the three PhC cases at $\alpha = \pm 0.25$ as examples. Figure 5 (a) and (b) present the extinction cross-sections of different multipoles for the even and odd quasi-BIC resonances in the first PhC case, and it is clearly seen that even quasi-BIC resonance is dominated by TD and MQ while odd quasi-BIC resonance is dominated by MD and EQ. More interestingly, this correlation between the parity and dominant multipole still holds for the other PhC cases as shown in Fig. 5(c-h).

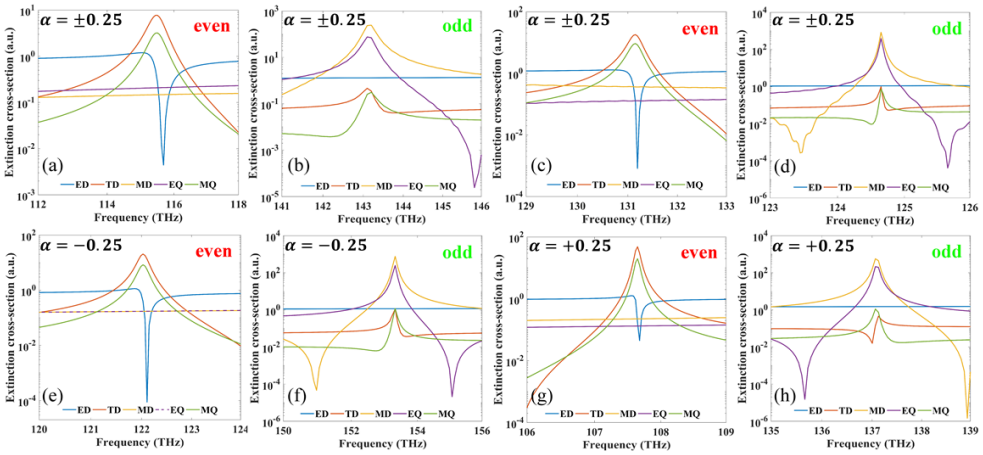

Fig. 5. The multipolar extinction cross-sections of even and odd quasi-BIC resonances for the three PhC cases. (a-b) The first PhC case at $\alpha = \pm 0.25$. (c-d) The second PhC case at $\alpha = \pm 0.25$. (e-f) The third case at $\alpha = -0.25$. (g-h) The third PhC case at $\alpha = +0.25$.

We further study the displacement current density and the magnetic field vector of these quasi-BIC resonances at $\alpha = 0.25$ to confirm their multipole dominations. For even quasi-BIC resonance in the first PhC case, the corresponding displacement current density and magnetic field vectors are visualized in Fig. 6(a) and (b), respectively. In the x-y plane, it is shown that displacement currents circulate counterclockwise between air holes in the upper position, while clockwise between air holes in the lower position, as indicated by red dash arrows. The magnetic field vectors in the y-z plane in Fig. 6(b) show that opposite-phase MDs form a closed magnetic vortex, possessing a counterclockwise circular manner as indicated by green dash arrows. Such a head-to-tail manner of magnetic field vectors is a characterization for the TD, which is also accompanied by the MQ [39]. For the odd quasi-BIC resonance, displacement currents circulate clockwise between intracellular air holes and counterclockwise between intercellular air holes in the x-z plane, as indicated in the lower figure of Fig. 6(c). As an example, the induced magnetic field vectors of the middle circular displacement currents in the y-z plane are shown in Fig. 6(d), of which direction is consistent with the right-hand screw rule. Such head-to-tail manner of displacement currents describes the MD. Meanwhile, the E_y distribution in the x-z plane can be identified as the EQ, as shown in the upper figure of Fig. 6(c). The third PhC case possesses results similar to this case when $\alpha = \pm 0.25$.

Similarly, For the even quasi-BIC resonance in the second PhC case, the displacement currents in the x-y plane circulate counterclockwise in areas below upper corner holes, whereas clockwise in areas above the lower corner holes, as given in Fig. 6(e). The induced opposite-phase MDs

Optics EXPRESS

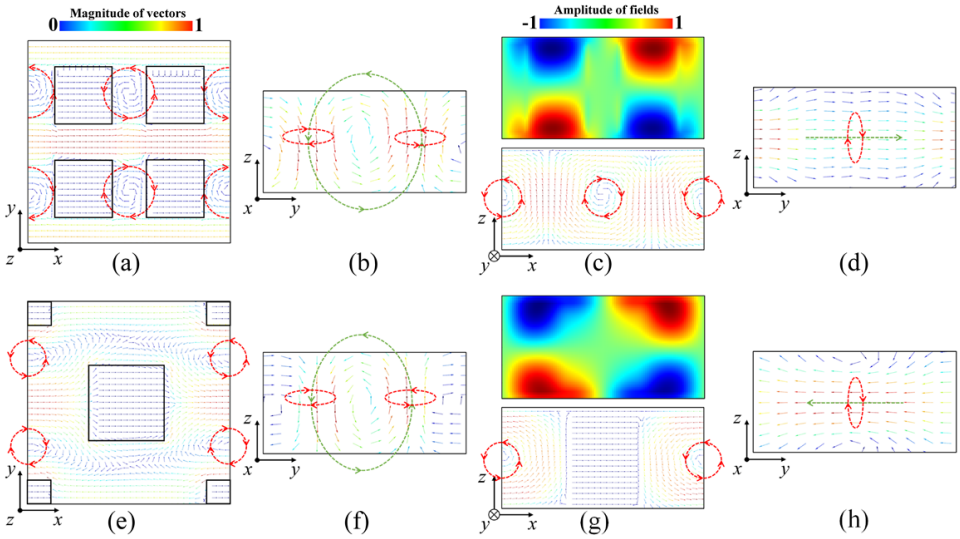

Fig. 6. (a,e) Displacement current density for the even quasi-BIC resonance in the first and second PhC cases at $\alpha = 0.25$, respectively. The color of the vector indicates the corresponding normalized magnitude, and red dash arrows indicate the flow of the displacement currents. (b,f) Magnetic field vectors for the even quasi-BIC resonance in the first and second PhC cases at $\alpha = 0.25$, respectively. Green dash arrows indicate the flow of the magnetic fields. (c,g) Upper: the E_y distribution for the odd quasi-BIC resonance in the first and second PhC cases at $\alpha = 0.25$, respectively. Lower: the corresponding displacement current densities. (d,h) Magnetic field vectors for the odd quasi-BIC resonance in the first and second PhC cases at $\alpha = 0.25$, respectively.

also form a closed magnetic vortex as shown in Fig. 6(f), leading to the TD and MQ. For the odd quasi-BIC resonance, we find that all displacement currents have a counterclockwise circular manner as shown in the lower figure of Fig. 6(g), and the corresponding magnetic field vectors are consistent with the right-hand screw rule as shown in Fig. 6(h), indicating the MD. The E_y distribution in the upper figure of Fig. 6(g) also reveals the existence of the EQ.

To explore the origin of the anomalous increase of the Q factor for even quasi-BIC resonances in the third PhC case, we further investigate their multipolar contributions at different α values, and the corresponding extinction cross-section values at resonant frequencies are plotted in Fig. 7(a). It is shown that the sharp rise of ED, TD, and MQ leads to the increase of the Q factor. As shown in Fig. 7(b), at $\alpha = -1$, displacement currents circulate clockwise and counterclockwise in the upper and lower positions of the x-y plane, respectively. In the lower figure of Fig. 7(c), the induced magnetic field vectors form multiple magnetic vortices in the y-z plane, leading to the TD and MQ. Besides, the E_y distribution in the x-z plane can be identified as the ED, as shown in the upper figure of Fig. 7(c). These features indicate that the even quasi-BIC resonance here has been transformed into another mode, which has not happened for the other cases with no anomalous behavior. Since this emerging mode is no longer the original quasi-BIC resonance governed by symmetry protection, it naturally does not follow the inverse quadratic law. For the odd quasi-BIC resonance, the corresponding multipolar contributions at different α values are shown in Fig. 7(d). It is shown that cross-sections of the MD, EQ, and ED vary gently with larger negative α, whereas the TD and MQ exhibit fluctuation, which further arouse the fluctuation of the Q factor.

Optics EXPRESS

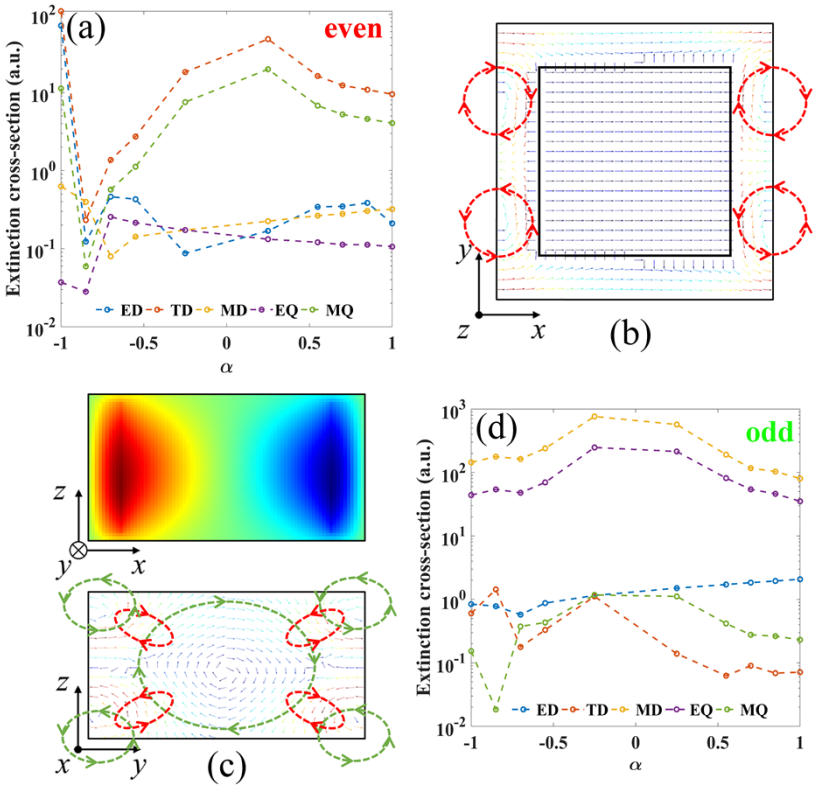

Fig. 7. (a,d) The multipolar extinction cross-sections of even and odd quasi-BIC resonances at resonant frequencies as a function of α for the third PhC case, respectively. (b) Displacement current density for the even quasi-BIC resonance in the third PhC case at $\alpha = -1$. (c) Upper: the E_y distribution for the even quasi-BIC resonance in the third PhC case at $\alpha = -1$. Lower: the corresponding magnetic field vectors.

6. Tailoring BICs with anisotropic coupling strengths

In the sections above, we only consider tuning intracellular and intercellular coupling strengths isotropically, i.e., Δd_a is equal in the x and y directions. In this section, we further investigate the effect of anisotropic coupling adjustment on BICs in our PhC slabs. Here, for the first PhC case in Fig. 2(a), we maintain d_a along the y direction, namely, d_{ay}, at 0.2 μm, and change d_{ax} continuously. Figure 8(a) shows that only odd quasi-BIC resonances appear. By contrast, only even quasi-BIC resonances emerge when d_{ay} varies while d_{ax} remains unchanged. Similar results also appear for the third PhC case, of which spectra are shown in Fig. 8(e) and (f), where we maintain d_{by} at 0.2 μm and change d_{bx} or vice versa. It is indicated that in both PhC cases, even BIC resonances are protected by the critical coupling along the y direction, whereas odd BIC resonances are protected by the critical coupling along the x direction.

However, distinct features appear for the second PhC case, where l_{ay} is maintained at 0.3 μm and l_{ax} varies or vice versa, meanwhile we keep $l_{ay(x)} + l_{by(x)} = 0.6$ μm. Figure 8(c) and (d) indicate that even and odd quasi-BIC resonances emerge for both cases, meanwhile possessing different frequency dispersion curves. It reveals that even and odd BIC resonances here are protected by the critical coupling in both x and y directions. Such anisotropic coupling adjustment enriches the means of tailoring BICs in our PhC slabs, and the separate tunability for the dual BICs has potential applications in double-resonant nonlinear enhancement [40].

Optics EXPRESS

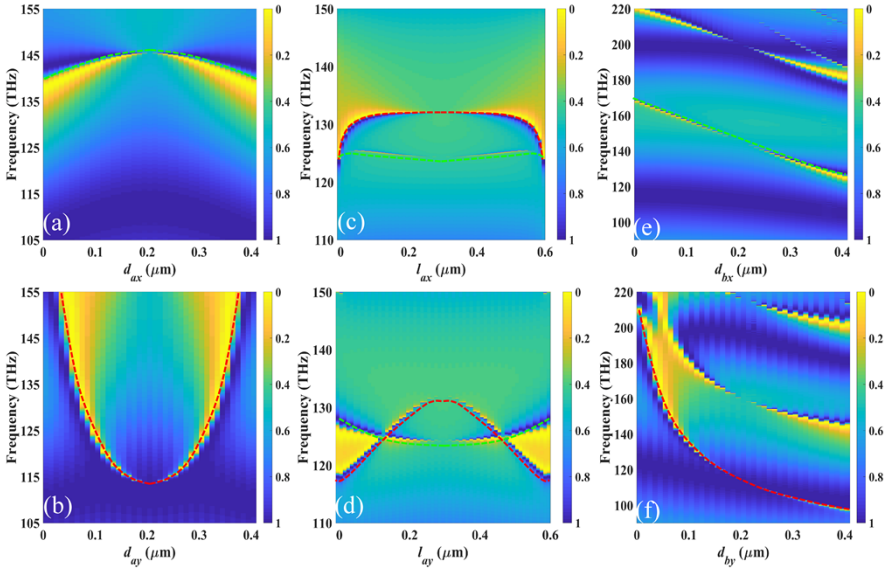

Fig. 8. The transmission spectra under anisotropic intracellular and intercellular coupling strengths for the three PhC cases. The red and green dash curves indicate the frequency dispersions of even and odd BIC resonances, respectively. (a-b) The first case where d_{ax} (d_{ay}) varies while d_{ay} (d_{ax}) remains unchanged at 0.2 μm. (c-d) The second case where l_{ax} (l_{ay}) varies while l_{ay} (l_{ax}) is maintained at 0.3 μm. Meanwhile the relation $l_{ay(x)} + l_{by(x)} = 0.6$ μm is kept. (e-f) The third case where d_{bx} (d_{by}) varies while d_{by} (d_{bx}) remains unchanged at 0.2 μm.

7. Conclusion

In summary, we theoretically investigate BIC and quasi-BIC resonances at Γ point based on four approaches to tune the coupling strength in PhC hole slabs. Since the unit cells in this work all possess C_4 symmetry, these resonances are intrinsically insensitive to the polarization direction of the incident plane wave, which is an advantage compared with BICs in symmetry-breaking metasurfaces. Further investigation shows that these resonances are the lowest-order even and odd modes that can match the symmetry of the plane wave. Notably, there is evidence, for example, in Fig. 8(e) and (f), that higher-order symmetry-match eigenmodes may also exist as BICs at Γ point, which is worth exploring in the future.

The inverse quadratic law can be applied for the Q factor distributions of these BIC and quasi-BIC resonances except for the PhC cases with large perturbations. To gain more insight, we implement the multipole decomposition, which reveals that even quasi-BIC resonances are governed by TD and MQ while odd quasi-BIC resonances are dominated by MD and EQ. In addition, the anomalous rise of the Q factor attributes to the transformation of the mode, because this mode is no longer the original symmetry-protected quasi-BIC resonance following the inverse quadratic law. It is worth mentioning that this does not mean that this mode is not associated with BICs since another type of BICs, resonance-trapped BICs, may also be supported at Γ point [21]. However, further exploration towards the nature of this mode is beyond the scope of this paper. Finally, we present that anisotropic coupling strengths can tailor BICs with more degrees of freedom. In Appendix B, we also discuss the influence of material losses and the substrate on resonances. This work introduces an approach to investigate Γ-point BICs from a different perspective, namely, from intra- and intercellular coupling strengths, and the proposed

Optics EXPRESS

PhC slabs can serve as high-Q cavities in planar photonic systems and have potential applications in double-resonant nonlinear enhancement, multi-spectral sensing, and lasing.

Appendix A: parity definition and eigenmode solutions

If one 3D PhC slab possesses one or more planes of reflection symmetry, the modes in it can be classified as even or odd modes as an analogue of transverse-magnetic (TM) and transverse-electric (TE) modes in 2D PhCs. In our PhC slabs, the horizontal mirror plane is the x-y plane at the middle of the slab where $z = 0$, thus the parity of mode is defined as follows [41]:

$$\begin{aligned}
\text{even}: &\begin{cases} E_x(x,y,z), E_y(x,y,z), E_z(x,y,z) = E_x(x,y,-z), E_y(x,y,-z), -E_z(x,y,-z) \\ H_x(x,y,z), H_y(x,y,z), H_z(x,y,z) = -H_x(x,y,-z), -H_y(x,y,-z), H_z(x,y,-z) \end{cases} \\
\text{odd}: &\begin{cases} E_x(x,y,z), E_y(x,y,z), E_z(x,y,z) = -E_x(x,y,-z), -E_y(x,y,-z), E_z(x,y,-z) \\ H_x(x,y,z), H_y(x,y,z), H_z(x,y,z) = H_x(x,y,-z), H_y(x,y,-z), -H_z(x,y,-z) \end{cases}
\end{aligned} \tag{4}$$

We further calculate the eigenmodes of our PhC slabs at $\alpha = 0.25$ with such parity classification at Γ point. Figure 9(a) presents the eigenmodes for the first PhC case, where H_z and E_z field profiles are shown in the insets for even and odd modes, respectively. We find that the first two even eigenmodes are degenerate and can match the symmetry of the plane wave, and the excited even quasi-BIC resonance belongs to the one marked with the pentagram. The other eigenmode can be excited if the polarization of the plane wave is rotated by 90°. For odd eigenmodes, the first two degenerate eigenmodes mismatch the symmetry of the plane wave, thus cannot be excited. However, the third odd eigenmode can meet the symmetry match, thus can be excited and actually is the odd quasi-BIC resonance. The fourth odd eigenmode is degenerate with the third one and can also be excited if the polarization of the plane wave is rotated by 90°. These explanations can also be applied for the other PhC cases, of which eigenmodes are shown in Fig. 9(b) and (c). Therefore, we conclude that the studied two BIC resonances in our PhC slabs are the lowest-order even and odd modes that can match the symmetry of the plane wave.

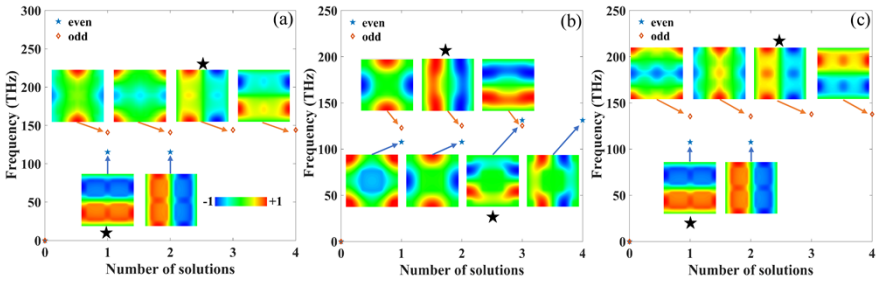

Fig. 9. Even and odd eigenmodes for the three PhC cases at $\alpha = 0.25$. The insets present H_z and E_z field profiles for even and odd modes at $z = 0$, respectively. The eigenmodes corresponding to excited quasi-BIC resonances are marked with pentagrams. (a) Eigenmodes of the first PhC case. (b) Eigenmodes of the second PhC case. (c) Eigenmodes of the third PhC case.

Appendix B: influences of material losses and the substrate

From a practical point of view, we investigate the influence of material losses on quasi-BIC resonances, which is not considered in the main text. Taking the first PhC case at $\alpha = 0.05$ as an example, we introduce the imaginary part into the permittivity of the slab so that $\varepsilon = 12 + i\varepsilon'$.

Optics EXPRESS

Figure 10(a) and (b) present the transmission spectra of even and odd quasi-BIC resonances at different imaginary part values, respectively. It is observed that the two resonances are gradually quenched with the increase of losses, and almost completely suppressed when $\varepsilon' = 10^{-1}$. Their Q factors with respect to losses are shown in Fig. 10(c) and (d), respectively, which indicate that the influence of losses can be neglected when $\varepsilon' \leq 10^{-5}$.

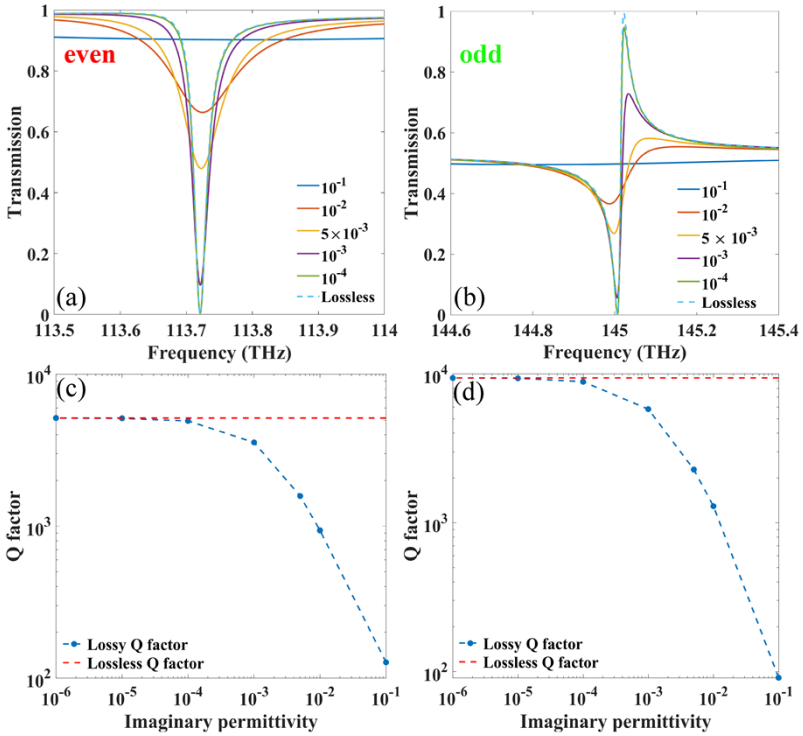

Fig. 10. (a-b) The transmission spectra of even and odd quasi-BIC resonances at different imaginary part levels, respectively. (c-d) The Q factor of even and odd quasi-BIC resonances at different imaginary part levels, respectively. Blue dots and red dash lines represent Q factors of lossy and lossless cases, respectively.

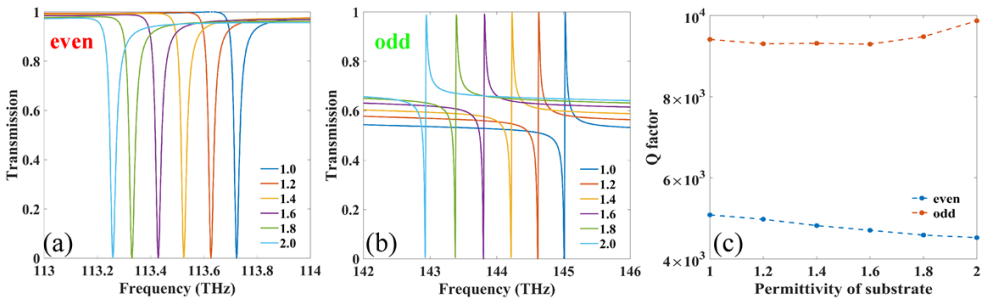

Fig. 11. (a-b) The transmission spectra of even and odd quasi-BIC resonances with respect to the permittivity of the substrate, respectively. (c) The Q factor of even and odd quasi-BIC resonances with respect to the permittivity of the substrate, respectively.

Optics EXPRESS

The substrate is essential for the experimental realization of this structure. To investigate its influence, a lossless dielectric substrate, whose permittivity will vary from 1.0 to 2.0, is introduced under the slab. Figure 11(a) and (b) show that the red shift occurs for the two quasi-BIC resonances with increasing permittivity of the substrate. Meanwhile, their line shapes are well maintained and the corresponding Q factors are merely perturbed, as depicted in Fig. 11(c). It further reveals that the two resonances are protected by the in-plane symmetry of the structure, and symmetry breaking along the z-axis will not destroy such protection. In practice, the slab and substrate can be made by Si and SiO_2, respectively, and the fabrication can be performed in a standard top-down approach [42].

Funding. National Natural Science Foundation of China (60907003, 61805278); National University of Defense Technology (JC13-02-13, ZK17-03-01); Natural Science Foundation of Hunan Province (13JJ3001); Program for New Century Excellent Talents in University (NCET-12-0142); Hunan Provincial Innovation Foundation for Postgraduate (CX20200039); Major Basic Research Project of the Natural Science Foundation of the Jiangsu Higher Education Institutions (20KJB140007).

Disclosures. The authors declare no conflicts of interest.

Data availability. Data underlying the results presented in this paper are not publicly available at this time but may be obtained from the authors upon reasonable request.

Supplemental document. See Supplement 1 for supporting content.

References

1. K. Totsuka, N. Kobayashi, and M. Tomita, "Slow light in coupled-resonator-induced transparency," Phys.Rev. Lett. **98**(21), 213904 (2007).
2. G. Lin, A. Coillet, and Y. K. Chembo, "Nonlinear photonics with high-Q whispering-gallery-mode resonators," Adv. Opt. Photonics **9**(4), 828–890 (2017).
3. R. Singh, W. Cao, I. Al-Naib, L. Cong, W. Withayachumnankul, and W. Zhang, "Ultrasensitive terahertz sensing with high-Q Fano resonances in metasurfaces," Appl. Phys. Lett. **105**(17), 171101 (2014).
4. M. Lončar, T. Yoshie, A. Scherer, P. Gogna, and Y. Qiu, "Low-threshold photonic crystal laser," Appl. Phys. Lett. **81**(15), 2680–2682 (2002).
5. D. T. Spencer, J. F. Bauters, M. J. R. Heck, and J. E. Bowers, "Integrated waveguide coupled Si3N4 resonators in the ultrahigh-Q regime," Optica **1**(3), 153–157 (2014).
6. X. Ji, F. A. S. Barbosa, S. P. Roberts, A. Dutt, J. Cardenas, Y. Okawachi, A. Bryant, A. L. Gaeta, and M. Lipson, "Ultra-low-loss on-chip resonators with sub-milliwatt parametric oscillation threshold," Optica **4**(6), 619–624 (2017).
7. Y. Yang, I. I. Kravchenko, D. P. Briggs, and J. Valentine, "All-dielectric metasurface analogue of electromagnetically induced transparency," Nat. Commun. **5**(1), 1–7 (2014).
8. J. Tian, Q. Li, P. A. Belov, R. K. Sinha, W. Qian, and M. Qiu, "High-Q all-dielectric metasurface: super and suppressed optical absorption," ACS Photonics **7**(6), 1436–1443 (2020).
9. Y. Akahane, T. Asano, B. S. Song, and S. Noda, "High-Q photonic nanocavity in a two-dimensional photonic crystal," Nature **425**(6961), 944–947 (2003).
10. M. S. Mohamed, A. Simbula, J.-F. Carlin, M. Minkov, D. Gerace, V. Savona, N. Grandjean, M. Galli, and R. Houdré, "Efficient continuous-wave nonlinear frequency conversion in high-Q gallium nitride photonic crystal cavities on silicon," APL Photonics **2**(3), 031301 (2017).
11. A. R. Alija, L. J. Martínez, A. García-Martín, M. L. Dotor, D. Golmayo, and P. A. Postigo, "Tuning of spontaneous emission of two-dimensional photonic crystal microcavities by accurate control of slab thickness," Appl. Phys. Lett. **86**(14), 141101 (2005).
12. M. Makarova, V. Sih, J. Warga, R. Li, L. Dal Negro, and J. Vuckovic, "Enhanced light emission in photonic crystal nanocavities with Erbium-doped silicon nanocrystals," Appl. Phys. Lett. **92**(16), 161107 (2008).
13. P. Jordan, J. von Neumann, and E. P. Wigner, in *The Collected Works of Eugene Paul Wigner* (Springer, 1993), pp. 298–333.
14. C. W. Hsu, B. Zhen, A. D. Stone, J. D. Joannopoulos, and M. Soljačić, "Bound states in the continuum," Nat. Rev. Mater. **1**(9), 1–13 (2016).
15. K. Koshelev, A. Bogdanov, and Y. Kivshar, "Meta-optics and bound states in the continuum," Sci. Bull. **64**(12), 836–842 (2019).
16. C. W. Hsu, B. Zhen, J. Lee, S. L. Chua, S. G. Johnson, J. D. Joannopoulos, and M. Soljačić, "Observation of trapped light within the radiation continuum," Nature **499**(7457), 188–191 (2013).
17. J. Jin, X. Yin, L. Ni, M. Soljačić, B. Zhen, and C. Peng, "Topologically enabled ultrahigh-Q guided resonances robust to out-of-plane scattering," Nature **574**(7779), 501–504 (2019).
18. K. Koshelev, S. Lepeshov, M. Liu, A. Bogdanov, and Y. Kivshar, "Asymmetric metasurfaces with high-Q resonances governed by bound states in the continuum," Phys. Rev. Lett. **121**(19), 193903 (2018).

Optics EXPRESS

19. Y. He, G. Guo, T. Feng, Y. Xu, and A. E. Miroshnichenko, "Toroidal dipole bound states in the continuum," Phys. Rev. B **98**(16), 161112 (2018).
20. J. F. Algorri, F. Dell'Olio, P. Roldán-Varona, L. Rodríguez-Cobo, J. M. López-Higuera, J. M. Sánchez-Pena, and D. C. Zografopoulos, "Strongly resonant silicon slot metasurfaces with symmetry-protected bound states in the continuum," Opt. Express **29**(7), 10374–10385 (2021).
21. A. I. Ovcharenko, C. Blanchard, J. P. Hugonin, and C. Sauvan, "Bound states in the continuum in symmetric and asymmetric photonic crystal slabs," Phys. Rev. B **101**(15), 155303 (2020).
22. V. R. Tuz, V. V. Khardikov, and Y. S. Kivshar, "All-dielectric resonant metasurfaces with a strong toroidal response," ACS Photonics **5**(5), 1871–1876 (2018).
23. P. Yu, A. S. Kupriianov, V. Dmitriev, and V. R. Tuz, "All-dielectric metasurfaces with trapped modes: Group-theoretical description," J. Appl. Phys. **125**(14), 143101 (2019).
24. Y. Cai, Y. Huang, K. Zhu, and H. Wu, "Symmetric metasurface with dual band polarization-independent high-Q resonances governed by symmetry-protected BIC," Opt. Lett. **46**(16), 4049–4052 (2021).
25. D. C. Zografopoulos and V. Dmitriev, "Quasi-dark resonances in silicon metasurface for refractometric sensing and tunable notch filtering," J. Lightwave Technol. **39**(21), 6985–6993 (2021).
26. W. Su, J. R. Schrieffer, and A. J. Heeger, "Solitons in polyacetylene," Phys. Rev. Lett. **42**(25), 1698–1701 (1979).
27. J. C. G. Henriques, T. G. Rappoport, Y. V. Bludov, M. I. Vasilevskiy, and N. M. R. Peres, "Topological photonic Tamm states and the Su-Schrieffer-Heeger model," Phys. Rev. A **101**(4), 043811 (2020).
28. M. Kim and J. Rho, "Topological edge and corner states in a two-dimensional photonic Su-Schrieffer-Heeger lattice," Nanophotonics **9**(10), 3227–3234 (2020).
29. B. Y. Xie, H. F. Wang, H. X. Wang, X. Y. Zhu, J. H. Jiang, M. H. Lu, and Y. F. Chen, "Second-order photonic topological insulator with corner states," Phys. Rev. B **98**(20), 205147 (2018).
30. F. Liu, H. Y. Deng, and K. Wakabayashi, "Topological photonic crystals with zero Berry curvature," Phys. Rev. B **97**(3), 035442 (2018).
31. H. R. Kim, M. S. Hwang, D. Smirnova, K. Y. Jeong, Y. Kivshar, and H. G. Park, "Multipolar lasing modes from topological corner states," Nat. Commun. **11**(1), 1–8 (2020).
32. S. G. Johnson, S. Fan, P. R. Villeneuve, J. D. Joannopoulos, and L. A. Kolodziejski, "Guided modes in photonic crystal slabs," Phys. Rev. B **60**(8), 5751–5758 (1999).
33. L. Cong and R. Singh, "Symmetry-protected dual bound states in the continuum in metamaterials," Adv. Opt. Mater. **7**(13), 1900383 (2019).
34. M. F. Limonov, M. V. Rybin, A. N. Poddubny, and Y. S. Kivshar, "Fano resonances in photonics," Nat. Photonics **11**(9), 543–554 (2017).
35. Z. Sadrieva, K. Frizyuk, M. Petrov, Y. Kivshar, and A. Bogdanov, "Multipolar origin of bound states in the continuum," Phys. Rev. B **100**(11), 115303 (2019).
36. R. Alaee, C. Rockstuhl, and I. Fernandez-Corbaton, "An electromagnetic multipole expansion beyond the long-wavelength approximation," Opt. Commun. **407**, 17–21 (2018).
37. J. F. Algorri, D. C. Zografopoulos, A. Ferraro, B. García-Cámara, R. Beccherelli, and J. M. Sánchez-Pena, "Ultrahigh-quality factor resonant dielectric metasurfaces based on hollow nanocuboids," Opt. Express **27**(5), 6320–6330 (2019).
38. T. Hinamoto and M. Fujii, "MENP: an open-source MATLAB implementation of multipole expansion for nanophotonics," OSA Continuum **4**(5), 1640–1648 (2021).
39. N. Papasimakis, V. A. Fedotov, V. Savinov, T. A. Raybould, and N. I. Zheludev, "Electromagnetic toroidal excitations in matter and free space," Nat. Mater. **15**(3), 263–271 (2016).
40. M. Minkov, D. Gerace, and S. Fan, "Doubly resonant χ (2) nonlinear photonic crystal cavity based on a bound state in the continuum," Optica **6**(8), 1039–1045 (2019).
41. J. D. Joannopoulos, S. G. Johnson, J. N. Winn, and R. D. Meade, *Molding the flow of light*, Princeton Univ. Press, Princeton, NJ [ua] (2008).
42. J. Jeong, M. D. Goldflam, S. Campione, J. L. Briscoe, P. P. Vabishchevich, J. Nogan, M. B. Sinclair, T. S. Luk, and I. Brener, "High quality factor toroidal resonances in dielectric metasurfaces," ACS Photonics **7**(7), 1699–1707 (2020).